ADVANCED MATERIALS INTERFACES
www.advmatinterfaces.de

Nanoporous-Gold-Polypyrrole Hybrid Materials for Millimeter-Sized Free Standing Actuators

Benedikt Roschning and Jörg Weissmüller*

This work studies the actuation of hybrid materials made from nanoporous gold, polypyrrole, and aqueous electrolyte. The deposition protocol affords a conformal polypyrrole coating on the entire internal interface of millimeter-sized nanoporous metal specimens made by dealloying. The hybrid material emerges when the remaining pore space is filled with perchloric acid. The metal serves as load-bearing and electronically conductive substrate, the polypyrrole as functional active component for actuation, and the aqueous electrolyte provides a pathway for fast ionic conduction. In this way, an actuator material is obtained that can be manufactured as monolithic bodies that can be subjected to compressive loads. Actuators with dimensions of millimeters in each spatial direction achieve characteristic times for actuation in the order of seconds and their work density is comparable to that of state-of-the-art piezoceramics. As a remarkable finding, the actuation strain scales with the square of the polypyrrole phase fraction. This is surprising in view of the linear scaling predicted by conventional micromechanical models. A micromechanical model that explains this behavior as the result of polypyrrole bridges that link adjacent struts of the metal skeleton is presented.

1. Introduction

It is well known that the electrically conductive polymer polypyrrole (PPy) reversibly exchanges ions with a surrounding electrolyte under control of the electrode potential, E, and that this process changes the volume of the polymer[1–8] in proportion to the transferred charge density, δq_V (charge per volume PPy).[2–4,9–12] Good environmental[13] and electrochemical cycling stabilities,[14] a low operating voltage[15] and strain amplitudes up to 40%[14,16–18] are exploited for actuation with PPy.[2,3,10,19,20] An important materials parameter of actuators is their strain-charge coupling coefficient, $\psi = \delta\varepsilon/\delta q_V$, where ε denotes the linear, uniaxial strain. For PPy, the magnitude and sign of ψ depend on the synthesis conditions, the species of transferred ions, the solvent and the mechanical boundary conditions.[4,5,11,21–23]

Besides the magnitude of the strain-charge coupling, the response time is an important characteristic of actuators. For PPy, the underlying charge transport kinetics include both, ionic transport and the formation of electronically conducting zones along the polymer chains.[24,25] If the potential interval is restricted so that the PPy is kept in its oxidized state with high electronic conductivity, the ion exchange is rate controlling. Similar to classical interdiffusion, the time constant for equilibration after a change in E increases with the square of the diffusion distance.[24–26] Acceptable response times thus require small actuator dimensions in at least one direction. Therefore, many studies investigate PPy as a thin film (typically not exceeding 10 µm) on an electrically conductive substrate. Examples for such actuators are bilayered bending cantilevers[27–29] which may exhibit roughened interfaces for enhanced adhesion,[30] multilayered axial strain actuators[31] or coated fibers spun to yarns.[10] Nanometer-thin PPy films allow for particularly fast reaction times.[15,32] For PPy films with a thickness of about 10 µm, the actuation response time increases to minutes.[33,34] Free-standing PPy actuators with a thickness of ≈100 µm and a cross-sectional gradient in microstructure have been investigated in the context of wireless actuation.[35,36] They exhibit similar response times. For even thicker geometries, the response will be prohibitively slow.

PPy actuators with spatial dimensions of mm or above can be realized with PPy-coated nanoskeleton structures, such as multi-walled carbon nanotube networks[37] or electrospun microribbons.[38] In these architectures, a liquid electrolyte in the pore space provides a fast pathway for long-range ion transport. Metal–PPy–electrolyte hybrid materials obtained by the imbibition of PPy-coated nanoporous metals[39] represent a particularly interesting case, because their skeleton structure is load-bearing under compression. This enables actuation against an external compressive load by free-standing macroscopic bodies without a supporting device structure. Furthermore, the mechanical behavior of nanoporous metals has been intensively studied.[40–45] This provides the opportunity for a

B. Roschning, Prof. J. Weissmüller
Institute of Materials Physics and Technology
Hamburg University of Technology
21073 Hamburg, Germany
E-mail: benedikt.roschning@tuhh.de
Prof. J. Weissmüller
Institute of Materials Research, Materials Mechanics
Helmholtz-Zentrum Geesthacht
21502 Geesthacht, Germany

The ORCID identification number(s) for the author(s) of this article can be found under https://doi.org/10.1002/admi.202001415.

© 2020 The Authors. Advanced Materials Interfaces published by Wiley-VCH GmbH. This is an open access article under the terms of the Creative Commons Attribution-NonCommercial-NoDerivs License, which permits use and distribution in any medium, provided the original work is properly cited, the use is non-commercial and no modifications or adaptations are made.

DOI: 10.1002/admi.202001415

meaningful discussion of the interaction between the stress and the strain in the active PPy component and the underlying skeleton structure. Understanding this interaction is required for an informed design strategy of the hybrid materials in order to optimize their actuation performance.

A nanoporous gold–PPy–electrolyte hybrid actuator has been demonstrated,[39] although with a skeleton with a comparatively large feature size of 250 nm. In view of the trend of the metal toward "smaller is stronger"[40–44] this implies a low strength. Furthermore, a detailed understanding of the micromechanics underlying the actuation of the hybrid material is missing.

Here, we report hybrid materials made of nanoporous gold (NPG) and PPy in which the metal skeleton has a mean strut or "ligament" size of 120 nm, providing enhanced strength. For 3D, mm-sized samples, we demonstrate a uniform, conformal PPy coating with actuation response times in the order of a few seconds. We discuss the micromechanics that links the macroscopic strain-charge coupling to recent data[23] of the stress-charge coupling of thin PPy films for the same counterion-solvent system. As a remarkable observation, rationalized by the micromechanics, we advertise the finding of a quadratic relation between the actuation strain and the PPy volume fraction.

2. Experimental Section

The NPG-PPy hybrid material was prepared in a dealloying processes followed by the electrodeposition of PPy as illustrated in **Figure 1**a. The master alloy, $Au_{25}Ag_{75}$, was obtained by melting Au (99.995%, Chempur) and Ag (99.99%, Chempur) in an arc melter.

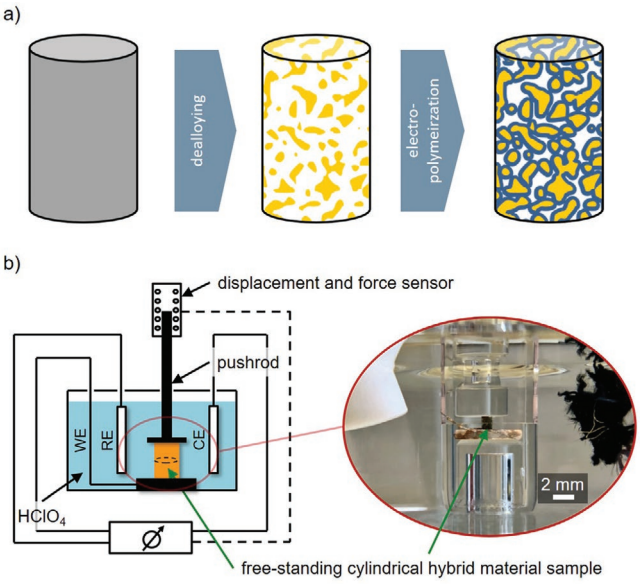

Figure 1. Sample preparation and experimental setup. a) The nanoporous gold polypyrrole hybrid material was made by dealloying a mm-sized gold-silver cylinder followed by the electrodeposition of polypyrrole. b) The nanoporous gold polypyrrole hybrid working electrode (WE), a reversible hydrogen reference electrode (RE), and a carbon counter electrode (CE) were immersed in electrolyte and connected to a potentiostat in a three electrode setup. The electrochemical cell was mounted in a dilatomter so that the length change of the working electrode was measured at a constant force of –300 mN.

The ingot was sealed in an evacuated quartz tube and homogenized for 120 h at 925 °C. A wire of 1.0 mm diameter was drawn and cut into cylinders of 1.8 mm length. For stress relief, the cylinders were annealed at 650 °C in a vacuum of 10^{-6} mbar for 1 h.

NPG was prepared by electrochemical dealloying at a constant potential of 0.75 V versus an Ag/AgCl pseudo reference electrode in 1 M $HClO_4$ (offset 0.53 V vs the standard hydrogen electrode, SHE).[46,47] After the dealloying current dropped below 20 µA, the potential was increased to 0.85 V in order to dissolve residual silver. Subsequently, the electrolyte was exchanged and the nanoporous specimens were subjected to 20 potential cycles between –0.4 and 1.1 V at a scan rate of 5 mV s^{-1}. The stop potential was 0.3 V, corresponding to a clean surface, free of adsorbed oxygen species.[48] The polarization at 0.85 V, the exchange of the electrolyte and the potential cycling were repeated once, resulting in NPG with a ligament size of $L = 40 \pm 5$ nm and a residual silver content below 1 at%.

To increase the ligament size, the samples were annealed in air at 300 °C for 10 min. The gold volume fraction is $\varphi_{Au} = 0.27 \pm 0.01$. L and the PPy layer thickness, d, were measured from scanning electron microscopy (SEM) images and are given as the average of ten individual values with the standard deviation as error.

Based on the procedures in refs. [23,39,49], PPy was deposited from a solution of 0.3 M pyrrole (98%, Sigma-Aldrich) and 0.3 M $LiClO_4$ (99.99%, Sigma-Aldrich) in acetonitrile (99.9%, Sigma-Aldrich) and 2 vol% ultrapure water (18.2 MΩ cm). A commercial Ag/AgCl electrode (in 3 M KCl, Metrohm) served as reference and a platinum mesh as counter electrode. The pyrrole was distilled at 130 °C and ambient pressure on the same day before deposition. The NPG substrate was subjected to 50 ms potential pulses of 800 mV with a wait time of 50 s at the open circuit potential between consecutive pulses. A detailed elaboration of the deposition protocol can be found in the Supporting Information.

All electrochemical characterization was performed in 1 M perchloric acid prepared from $HClO_4$ (Suprapure, Merck) and ultrapure water (18.2 MΩ cm), deareated with argon. A reversible hydrogen electrode (Gaskatel, HydroFlex) served as reference and a carbon cloth as counter electrode. All potentials in this work are specified versus the SHE, unless otherwise stated. The capacitive charging was characterized by a potentiostat (Metrohm, Autolab PGSTAT 302N). A linear scan generator allowed a continuous current measurement which is necessary for precise integration of the transferred electric charge.

For the electrochemical actuation experiments, an electrochemical cell was mounted in a dilatometer (Linseis, L75) as shown by the schematics in Figure 1b. The strain was measured as the relative length change of the mm-sized cylindrical body of the hybrid material. To contact the NPG-PPy specimen to the potentiostat as working electrode, the sample was supported by a gold plate. A constant contact force of –300 mN was applied. Throughout this work, the sign convention that all forces and displacements in compressive direction are negative is followed.

To determine the strain-charge coupling coefficient in various states of plastic deformation, the electrochemical cell was mounted in a loadframe instrument (ElectroForce, 3200 Series) in the same manner as in the dilatometer. The load or the displacement could be alternatively controlled, while both parameters were recorded. The specimens were plastically

© 2020 The Authors. Advanced Materials Interfaces published by Wiley-VCH GmbH

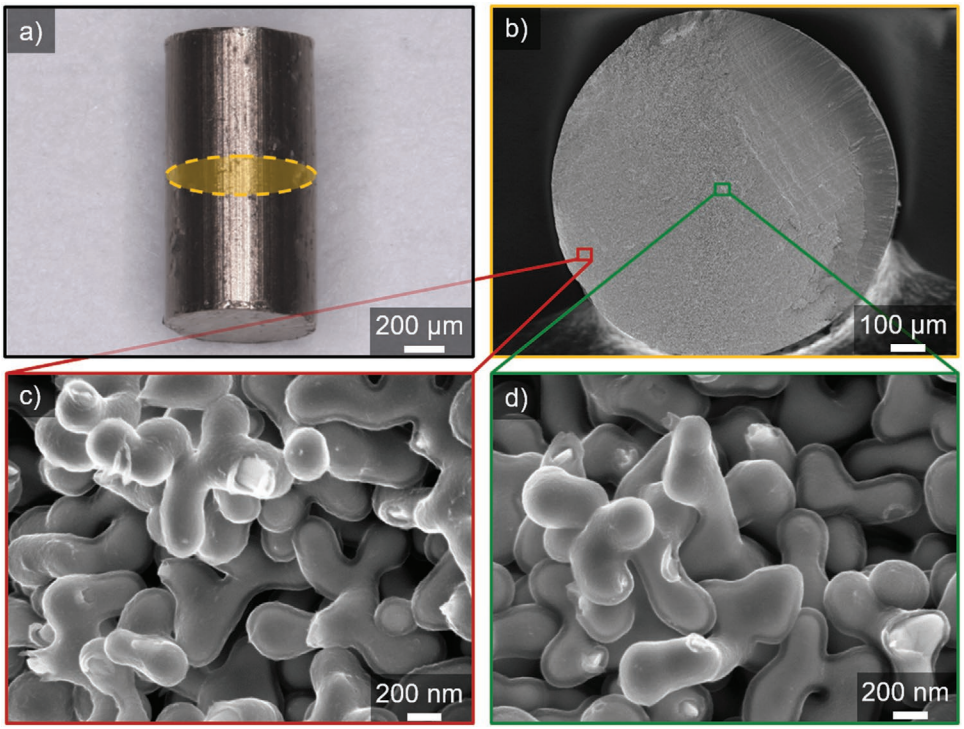

Figure 2. Micrographs of a nanoporous gold-polypyrrole hybrid actuator. 600 deposition cycles with 50 ms deposit pulses at 800 mV relative to a Ag/AgCl reference electrode with 50 s breaks between consecutive pulses; ligament size: $L = 120 \pm 10$ nm. a) Macroscopic specimen, 1 mm in diameter and 1.8 mm in length. b) Cross-sectional overview as highlighted in a). c) Magnified image section at the edge; film thickness: $d = 39 \pm 3$ nm. d) Magnified image section at the center; film thickness: $d = 32 \pm 3$ nm.

deformed with a strain rate $\dot{\varepsilon} = 10^{-4}$ s^{-1} to a predefined target strain. Afterward, they were unloaded at the same rate until a clamping force of –500 mN was reached. The clamping force was held constant and the length change was measured while the electrode potential was varied. Consecutive repetition with increasing prestrain results in stress–strain curves with interposed unloading segments. The yield strength, σ_Y, Young's modulus, Y, and the strain-charge coupling coefficient, A^*, varied as a function of the pre-strain. Their magnitudes were measured as function of the plastic strain, ε_{plast}, in other words, the strain after unloading. Young's modulus was determined by the secant over the unloading segments and σ_Y was identified as the stress at the onset of unloading.

3. Microstructure and Polypyrrole Film Thickness

Figure 2a,b depict a specimen after 600 polymerization cycles and a cross-sectional cleavage surface, as highlighted by the shaded area, respectively. Figure 2c,d picture magnified areas at the edge and at the center of the specimen, respectively. The ligament size is uniform over the cross-section and takes the value, $L = 120 \pm 10$ nm. We find a quite uniform PPy film thickness, d, of 39 ± 3 nm at the edge and 32 ± 3 nm at the center. Furthermore, neither overcoating of the sample nor coating of the counter electrode was observed.

Figure 3 shows magnified views of fracture surfaces for specimens after 400, 600, and 800 deposition cycles. The cumulative deposition times, t_c, were 20, 30, and 40 s, respectively. It can be seen that the film thickness, $d(t_c)$, increases with increasing t_c. Our analysis yields $d(20\,\text{s}) = 18 \pm 1$ nm, $d(30\,\text{s}) = 32 \pm 1$ nm, and $d(40\,\text{s}) = 42 \pm 1$ nm.

Figure 4 plots d at the center and the outer edge of the cleavage surface versus t_c for different samples. It can be seen that d increases linearly with t_c and that d in the center and at the edge are in excellent agreement. To show that the pulse length of 50 ms is sufficiently short, additional data points for a specimen manufactured with a pulse length of 30 ms and 400 deposition cycles were added. The additional data points match the linear trend. Linear regression of the data in Figure 4 yields a slope of

$$\frac{d}{t_c} = (0.99 \pm 0.02)\frac{\text{nm}}{\text{s}} \quad (1)$$

with the standard error as uncertainty.

4. Electrochemistry and Actuation

4.1. Electrochemical Characterization

In order to avoid a nonrecoverable (faradaic) charge transfer due to water splitting under cathodic conditions or degradation of the PPy due to overoxidation under anodic conditions,[50] the vertex potentials of our electrochemical potential cycles were chosen as 0.1 V and 0.9 V versus SHE. **Figure 5**a shows cyclic voltammograms (CVs) of the current density, i_V^*, (per outer sample volume) versus the electrode potential, E, for specimens

© 2020 The Authors. Advanced Materials Interfaces published by Wiley-VCH GmbH

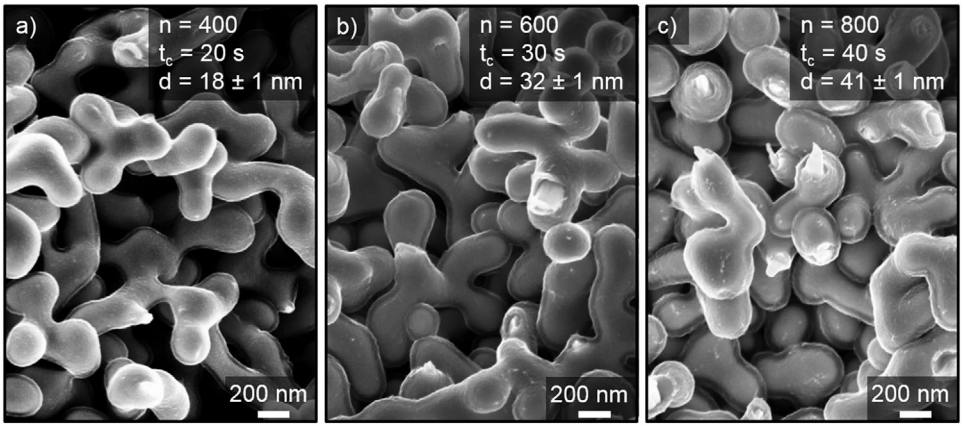

Figure 3. Film thickness evolution in the center of nanoporous gold-polypyrrole hybrid actuators. *n*: number of deposition cycles; t_c: cumulative deposition time; *d*: film thickness. a) $n = 400$, b) $n = 600$, c) $n = 800$.

with cumulative deposition times of t_c = 0, 10, 20, 30, and 40 s, respectively. The potential sweep rate was $\dot{E} = 10\,\mathrm{mV\,s^{-1}}$. The rectangular appearance of the CVs suggests capacitive or pseudo-capacitive behavior.[51] This finding is consistent with previous observations[11,23] which locate the present potential range in the oxidized regime.

The differential volumetric capacitance can be defined as $c_V^* = \delta q_V^* / \delta E = \hat{i}_V^* / \dot{E}$, where q_V^* denotes the volumetric charge density and all densities are referred to the outer sample volume. Here, we took $\hat{i}_V^*$ as the averaged current density in the potential interval 0.3–0.7 V and plotted the results for c_V^* in Figure 5b. The graph shows c_V^* versus t_c for all specimens under study. Linear regression yields $c_V^*/t_c = 2.35 \pm 0.08\,\mathrm{mF\,mm^{-3}\,s^{-1}}$, with the standard error as uncertainty. The capacitance of PPy depends on the synthesis conditions and on the nature of the co-ion. It takes on values in the order of magnitude of $0.1\,\mathrm{F\,mm^{-3}}$.[5,23,52,53] The PPy/co-ion system under study has a volume specific capacitance of $c_V = 0.24 \pm 0.01\,\mathrm{F\,mm^{-3}}$.[23] As an adaptation of the capacitance ratio method,[54] we used the ratio of c_V^* over c_V to determine the PPy volume fraction per outer sample volume, φ_{PPy}. φ_{PPy} can then be linked to the cumulative deposition time via

$$\varphi_{PPy} = (9.79 \pm 0.38) \times 10^{-3}\,\mathrm{s^{-1}}\, t_c \quad (2)$$

For the data set of Figure 5a, the PPy volume fractions emerge as φ_{PPy} = 0, 9, 18, 30, and 45%, respectively.

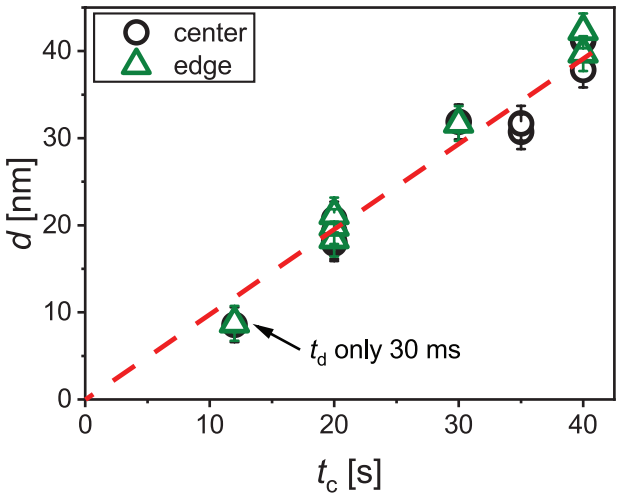

Figure 4. Evaluation of the film thickness. Polypyrrole layer thickness, *d*, versus cumulative deposition time, t_c. Except for the individually marked data points, all specimens were manufactured with a deposition pulse length of $t_d = 50$ ms. Dashed line: straight line of best fit.

4.2. In Situ Strain Measurements

We studied the actuation during cyclic voltammetry for the same specimens as in Figure 5a, within the same potential interval and at the same scan rate. **Figure 6**a shows the resulting variation of the uniaxial actuation strain, ε, with time during potential cycling. It can be seen that the strain is reversible and that the peak-to-peak strain amplitude, ε_{max}, increases with increasing φ_{PPy}. The strain amplitude of the hybrid material reaches up to $\varepsilon_{max} = 4.8 \times 10^{-3}$. This is more than two orders of magnitude larger than the strain amplitude of the bare NPG samples in our study. For those samples, we found $\varepsilon_{max} = 4.7 \times 10^{-5}$. An evaluation by SEM after potential cycling showed no signs of degradation or delamination of the PPy layer (see Figure S2, Supporting Information).

Figure 6b plots ε_{max} versus φ_{PPy} for all specimens under study. The dashed line represents a fit with a parabola, $\varepsilon_{max} = a\varphi_{PPy}^2$, with the parameter *a* adjusted for best fit. The agreement with the data shows that remarkably, and unlike the capacitance, the strain amplitude increases quadratically with φ_{PPy}.

Figure 7 combines the strain data with the electrochemical characteristics. Figure 7a plots the transferred charge density per volume PPy, $\Delta q_V = \Delta q_V^* / \varphi_{PPy}$, over the potential. Apart from a small hysteresis, Δq_V varies linearly and reversibly with *E*. The charge graphs are perfectly closed, indicating that the transferred charge is recoverable. Furthermore, the graphs superimpose. This notion is consistent with our scaling approach and a linear relation between c_V^* and φ_{PPy}.

Figure 7b plots the scaled strain, $\varepsilon/\varphi_{PPy}^2$, versus the potential. This reflects our earlier observation of a quadratic increase in strain amplitude with φ_{PPy}. In agreement with this observation,

© 2020 The Authors. Advanced Materials Interfaces published by Wiley-VCH GmbH

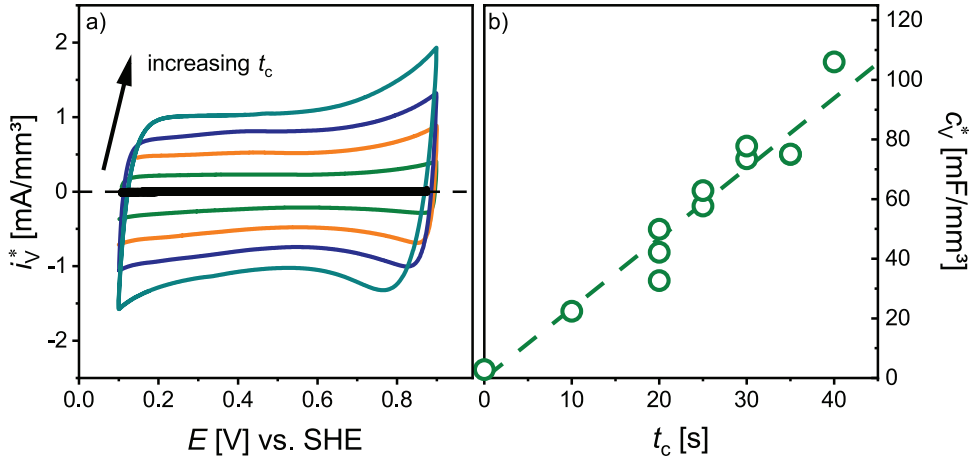

Figure 5. Characterizing the capacitance. a) Exemplary cyclic voltammograms of the volumetric current density, i_V^*, versus the electrode potential, E, measured relative to the standard hydrogen electrode (SHE) at a sweep rate, $\dot{E}$, of 10 mV s^{-1}. Color of graphs refers to specimens that vary in volume content of polypyrrole as consequence of an increased cumulative deposition time, t_c. The deposition time varied from 0 to 40 s. b) Corresponding volumetric capacitance, c_V^*, versus t_c. Dashed line: Linear regression. Black line in a) and $t_c = 0$ in b) refer to bare nanoporous gold.

the graphs superimpose. It is seen that the variation is roughly linear, and that there is a small but noticeable hysteresis.

Figure 7c plots the scaled strain versus the charge density. While a small nonlinearity persists, the hysteresis has vanished. The linear relation between the scaled strain and charge density is in line with the well-established notion that the actuation as well as the charge transfer are governed by the same fundamental process—the exchange of ions between the polymer and the surrounding electrolyte.[1–6,21]

4.3. Actuation Coefficient

As a figure of merit, the actuation coefficient, A^*, is defined as the derivative of the macroscopic, linear strain with respect to the volumetric charge density[39]

$$A^* = \frac{\delta\varepsilon}{\delta q_V^*} \tag{3}$$

We estimated A^* from the slope of the linear section of graphs such as Figure 7c. **Figure 8** shows A^* over φ_{PPy} for all specimens under study. The figure combines data from dilatometry and from experiments with the load frame instrument which are found to be consistent. It can be seen that A^* varies linearly with φ_{PPy}. Linear regression yields the slope

$$A^* = (0.14 \pm 0.01)\,\frac{\mathrm{mm}^3}{C}\,\varphi_{PPy} \tag{4}$$

with the standard error as uncertainty.

4.4. Strain Charge Coupling of Specimens Densified by Plastic Deformation

The structure of our hybrid material can be modified via densification by uniaxial plastic deformation. This provides an additional parameter for tailoring its properties. Furthermore, the exploration

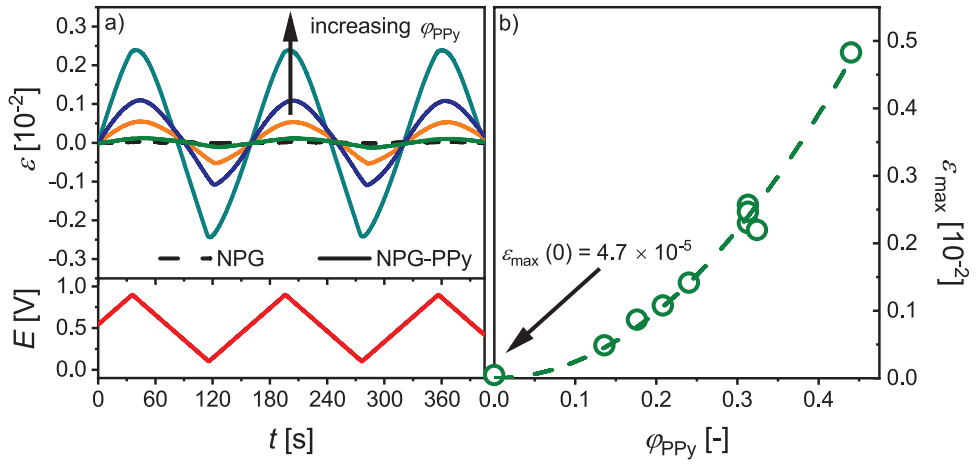

Figure 6. Actuation measurements. a) Exemplary strain-, ε, time curves during cyclic voltammetry with different volume fractions of polypyrrole, φ_{PPy}. b) Peak-to-peak strain amplitude, ε_{max}, versus φ_{PPy}. Dashed line: Fit with a parabola.

© 2020 The Authors. Advanced Materials Interfaces published by Wiley-VCH GmbH

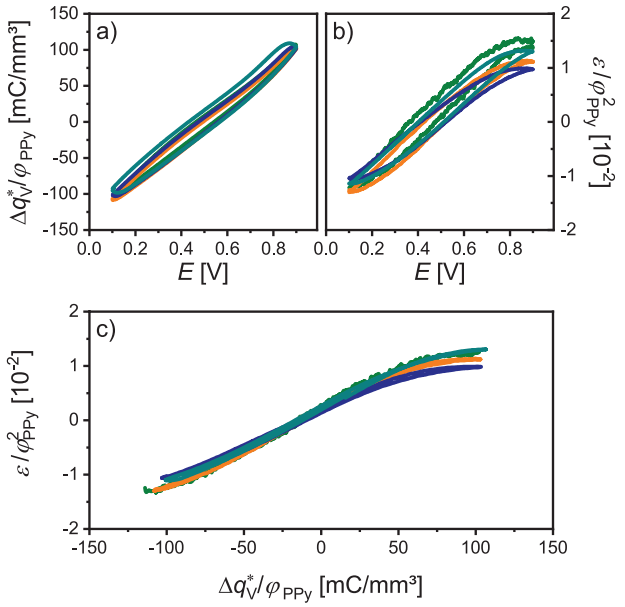

Figure 7. Characterizing the electrochemical actuation. In situ actuation study for exemplary specimens with volume contents of polypyrrole, φ_{PPy} from 9 to 45% during cyclic voltammetry. Potential sweep rate $\dot{E} = 10\,\text{mV s}^{-1}$. a) Scaled transferred charge density (charge per sample volume), $\Delta q_V^*/\varphi_{PPy}$, over the potential, E. b) Scaled strain, $\varepsilon/\varphi_{PPy}^2$, versus E. c) $\varepsilon/\varphi_{PPy}^2$ versus $\Delta q_V^*/\varphi_{PPy}$.

of the electrochemical actuation as function of the plastic deformation provides insights into the actuation mechanisms. This is particularly significant if the actuation of one and the same specimen is investigated in different states of densification.

Densification was achieved by loading the specimen beyond its yield stress. Load–unload cycles supplied the yield strength and Young's modulus of the material in its respective state of densification. The actuation was characterized at no load, in-between unloading and reloading. The densification-unloading-actuation-reloading sequence was repeated several times on any given specimen, yielding actuation data for the same specimen at different densities.

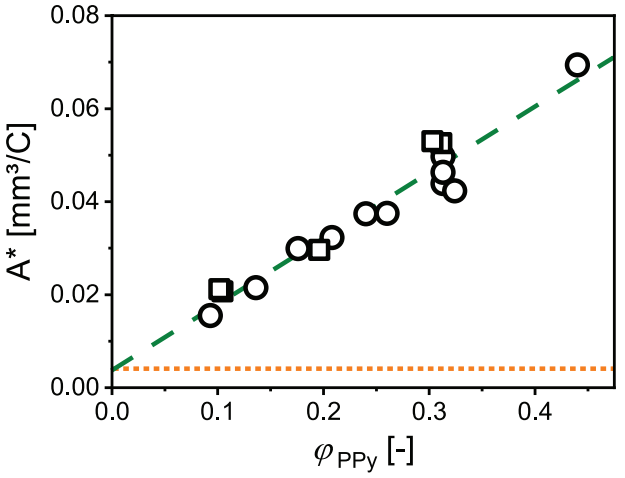

Figure 8. Characterizing the strain charge response. Strain charge coupling coefficient, A^*, versus the volume fraction of polypyrrole, φ_{PPy}. Circles: Data obtained by dilatometery. Squares: Data obtained with the loadframe instrument. Dashed line: Straight line of best fit. Dotted line: Estimate by Equation (9) considering only axial straining of the ligaments.

Figure 9a shows stress–strain curves interspersed with unloading segments for specimens with φ_{PPy} = 0.00, 0.10, 0.20, 0.25, and 0.30, respectively. It can be seen that the flow stress at any given strain increases with φ_{PPy}. In other words, the coating of the NPG skeleton with PPy results in a substantial strengthening. Figure 9b plots the yield strength, σ_Y, against the plastic deformation, ε_{plast}, for the different samples. The magnitude of σ_Y increases with both, ε_{plast} and φ_{PPy}. The largest strength exceeds 30 MPa, fivefold larger than the 6 MPa reported in[39] for a NPG-based hybrid material with a larger ligament size of 250 nm.

It is well known for NPG with L in the order of 100 nm, that the specimens immediately start to yield upon loading.[40,42–44,55] Therefore, Young's modulus, Y, could not be determined at the initial state. Figure 9c plots Y against ε_{plast}. Like the yield strength, Y is seen to increase with ε_{plast} and φ_{PPy}. The NPG reference sample has a lower initial stiffness than the NPG-PPy hybrids, with a substantially stronger increase in Y with ongoing plastic deformation.

Finally, Figure 9d plots A^* over ε_{plast}. The observations at zero plastic strain confirm our findings from the previous subsection by attributing a finite actuation coefficient to bare NPG and an increase of A^* with increasing φ_{PPy}. Yet, while A^* of bare NPG is essentially unaffected by the densification (here, $A^* = 0.024 \pm 0.002\,\text{mm}^3\,\text{C}^{-1}$), A^* of the hybrid materials increases significantly with ongoing densification.

4.5. Response Time

Figure 10 depicts the strain variation, $\Delta\varepsilon$, over time after the potential was stepped from 0.9 to 0.1 V and held constant for specimens with φ_{PPy} = 0.28, 0.37, and 0.44, respectively. For the sake of clarity, only the contraction reaction is shown, the transients for expansion and contraction reactions are similar. The response rates—parameterized by the time, $t_{1/2}$, required to reach half the saturation strain—are 1.5, 2.0, and 3.3 s, respectively.

5. Discussion

5.1. Film Thickness and Polypyrrole Volume Fraction

Our study is based on in situ strain measurements during potential cycling, investigating NPG-PPy hybrids with varying volume fractions of PPy. The PPy coating was characterized by two independent methods: a) the PPy-film thickness was extracted from scanning electron micrographs. b) the PPy volume fraction was determined by the electrochemical capacitance ratio method.

In order to compare these two methods, we consider the substrate–electrolyte interface during PPy film growth. As the PPy deposition progresses, the contact area between the PPy surface and the electrolyte increases due to the cylindrical shape of the ligaments. This apparent increase in substrate surface area competes with a decrease as result of the formation of new contacts between adjacent ligaments and the smoothing of saddle-shaped regions which abound in the nanoporous structure.[56,57]

© 2020 The Authors. Advanced Materials Interfaces published by Wiley-VCH GmbH

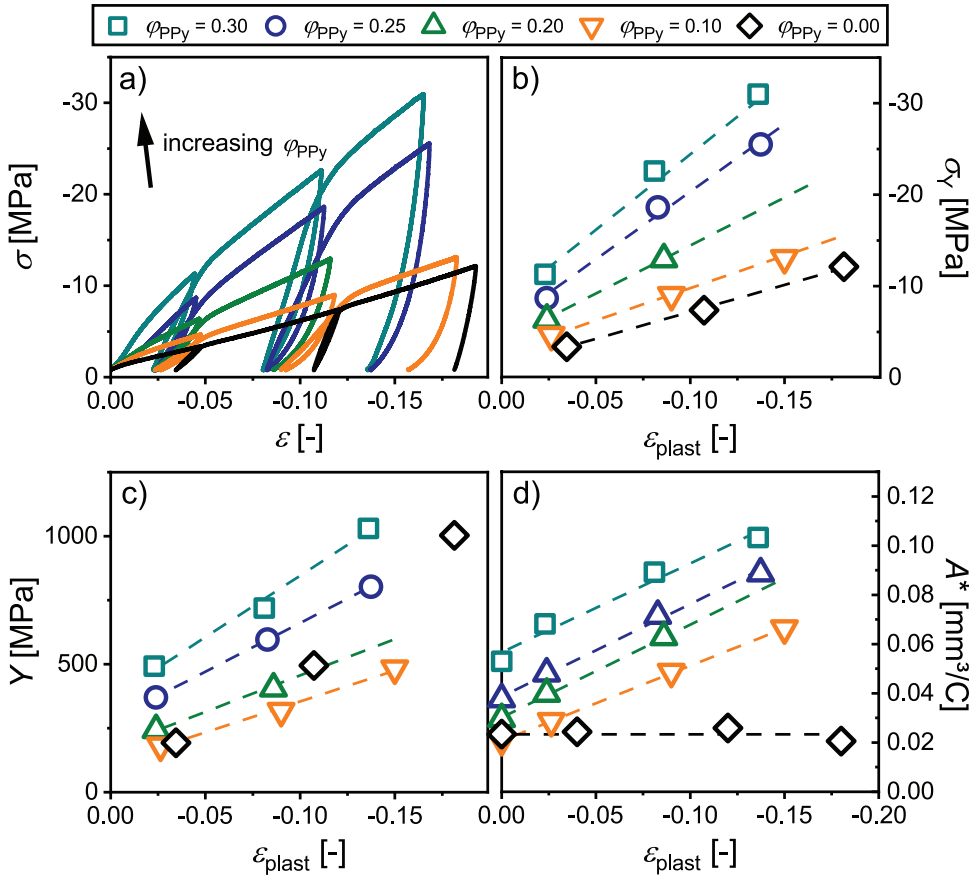

Figure 9. Characterizing the mechanical properties and the actuation behavior after predeformation. a) Stress-, σ, strain, ε, curves for specimens with varying volume fraction of polypyrrole, φ_{PPy}. b) Young's modulus, Y, versus plastic strain, ε_{plast}. c) Yield strength, σ_Y, versus ε_{plast}. d) Strain-charge coupling coefficient, A^*, versus ε_{plast}.

The polymerization was performed in short potentiostatic pulses in order to avoid monomer depletion within the pore space. While the coating thickness increases, we expect in each pulse a constant amount of deposited PPy per area, S, of surface. If the footprint area would change drastically during the polymerization process, the amount of deposited PPy and consequently the capacitance of the specimen would vary non-linearly with the deposition time. This consideration is in contrast to the experimentally observed proportionality between the capacitance and the cumulative deposition time, as shown in Figure 5b. Therefore, it is reasonable to assume that the interface between the substrate and the electrolyte remains essentially constant during the PPy deposition. The PPy volume fraction can then be expressed as

$$\varphi_{PPy} = \frac{Sd}{V} \tag{5}$$

With the time-thickness proportionality from Equation (1) and the ratio between the intrinsic surface area and the sample volume (Equation (S3), Supporting Information), φ_{PPy} can be expressed as function of t_c

$$\varphi_{PPy} = 4 \times (0.99 \pm 0.01) \frac{\text{nm}}{\text{s}} \frac{\varphi_{Au}}{L} t_c = K t_c \tag{6}$$

With $L = 120 \pm 10$ nm and $\varphi_{Au} = 0.27$, Equation (6) yields the slope $K = (8.91 \pm 0.91) \times 10^{-3}\ \text{s}^{-1}$ which is in good

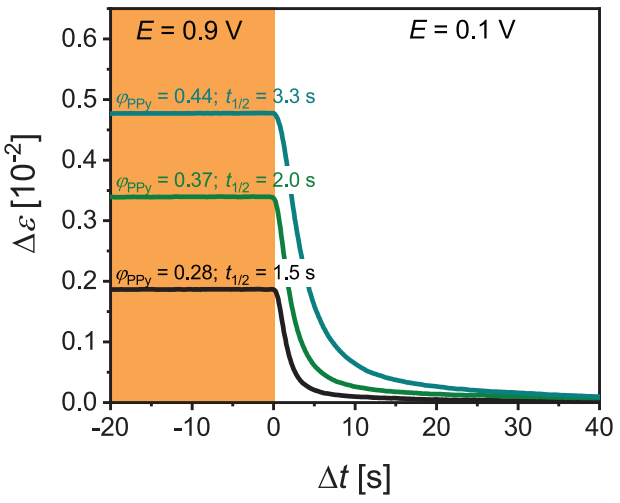

Figure 10. Strain response to potential steps. Strain variation, $\Delta\varepsilon$, versus time, t, for potential steps from 0.9 to 0.1 V versus the standard hydrogen electrode for specimens with polypyrrole volume fractions, φ_{PPy} = 0.28, 0.37, and 0.44, respectively.

© 2020 The Authors. Advanced Materials Interfaces published by Wiley-VCH GmbH

agreement with the electrochemical determined result of $(9.79 \pm 0.38) \times 10^{-3}\ s^{-1}$ (Equation (2)). The consistency of the results from the two independent methods supports our experimental finding for φ_{PPy}.

5.2. Actuation and Strain-Charge Coupling

The actuation mechanism of uncoated NPG has been linked to the electrocapillarity of gold electrode surfaces.[58] When such electrodes are polarized, their surface stress, f, varies. The underlying electrocapillary coupling coefficients are well documented.[59–61] Compensating stresses in the subjacent bulk deform the metal skeleton and the axial component of the strain in each ligament propagates along the network and thereby produces the macroscopic actuation strain.[62]

An investigation of the electromechanical coupling of planar PPy-coated gold electrodes with similar film thicknesses as in the present study revealed that the potential drop at the electrode is completely localized within the PPy.[23] Therefore, the metal is not polarized and its electrocapillary coupling can be ignored. Instead, tangential stresses in the PPy film are responsible for the deformation of the underlying planar substrate. By analogy to the observations on planar surfaces, the most obvious actuation mechanism of our hybrid materials would be the axial straining of the Au ligaments in response to the tangential stresses which develop in the clamped PPy coating when ions are exchanged with the surrounding electrolyte.

The contribution of the above mechanism to the actuation coefficient is readily estimated: As derived in ref. [62], the uniaxial straining of a network of gold ligaments can be expressed as function of the surface stress

$$\delta\varepsilon = -\frac{1-\nu_{Au}}{Y_{Au}}\frac{S}{\varphi_{Au}V}\delta f \tag{7}$$

Y_{Au} and ν_{Au} denote Young's modulus and Poisson's ratio of bulk gold, respectively. The stress-charge coupling coefficient of the clamped PPy film

$$\xi = \frac{\delta\sigma}{\delta q_V} \tag{8}$$

relates the tangential film stress, σ, to the transferred charge density (per volume of the polymer), q_V.[23] The variation in surface stress, δf, acts in the same way as the variation of the stress-thickness product in the PPy film, $d\,\delta\sigma$. In view of Equation (8), we may substitute $\xi_{PPy}\,d\,\delta q_V$ for that term. With the definition of A^* from Equation (3) and the assumption of a constant PPy surface area during deposition (Equation (5)), Equation (7) yields

$$A^* = -\frac{1-\nu_{Au}}{Y_{Au}}\frac{\xi_{PPy}}{\varphi_{Au}} \tag{9}$$

Note that A^* emerges as independent of the PPy phase fraction φ_{PPy}. In other words, this scenario is not compatible with the linear variation of A^* with φ_{PPy} as shown in Figure 8.

With $Y_{Au} = 79\,GPa$ and $\nu_{Au} = 0.42$[63] as well as $\xi_{PPy} = -153 \pm 11\,mV$[23] and $\varphi_{Au} = 0.27$, Equation (9) yields $A^* = (4.16 \pm 0.30) \times 10^{-3}\,mm^3\,C^{-1}$. At first sight, this result strikes as considerably smaller than the experimental data of Figure 8. Yet, when the estimate of A^* is plotted along with that data (see the dotted line in Figure 8), it can be seen that it reproduces the strain charge-coupling in the limit of $\varphi_{PPy} \to 0$. In other words, our observations in the limit of very thin films appear consistent with the estimate for the actuation strength based on tangential stresses alone. The deviation at finite φ_{PPy} implies that the actual deformation mechanism has an additional contribution which is not captured by the simple axial straining of the ligaments as a consequence of the stress development in the constrained PPy film.

The failure of a model based exclusively on the axial deformation of the ligaments in the NPG skeleton leads us to the investigation of an additional contribution, namely the expansion of the PPy normal to the substrate surface. If—as we have tacitly assumed so far—no contacts between the PPy coating of neighboring ligaments exist, the normal strain would have no effect on the external volume change. Yet, the latter assumption appears inappropriate, especially if larger PPy phase fractions are considered. In fact, we regularly observed contacts in electron micrographs of the hybrid material. This observation is exemplified in **Figure 11** which shows another micrograph of the cleavage surface depicted in Figure 3b. Circles highlight features where the fracture occurred along the gold-PPy interface. Peel-off tests revealed that PPy films delaminate from gold substrates.[30,64] Therefore, the location of the fracture at the interface is expected.

The above observations can only be understood if one admits that neighboring ligaments can be connected through PPy bridges. The inset in the figure provides a schematic illustration of such connections. As an additional feature, the coating may reconnect "dangling" ligaments of the skeleton structure. Such disconnected ligaments appear, if NPG with an initial

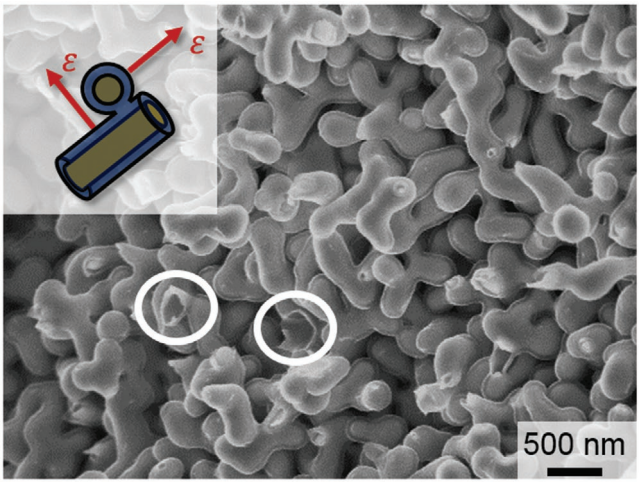

Figure 11. Fracture surface of a nanoporous gold-polypyrrole hybrid actuator. The circled dome shaped features show regions where the fracture appeared in the interface gold-PPy. Inset: Sketch demonstrating the actuation mechanism which results from the normal deformation in the newly formed connection between adjacent ligaments.

© 2020 The Authors. Advanced Materials Interfaces published by Wiley-VCH GmbH

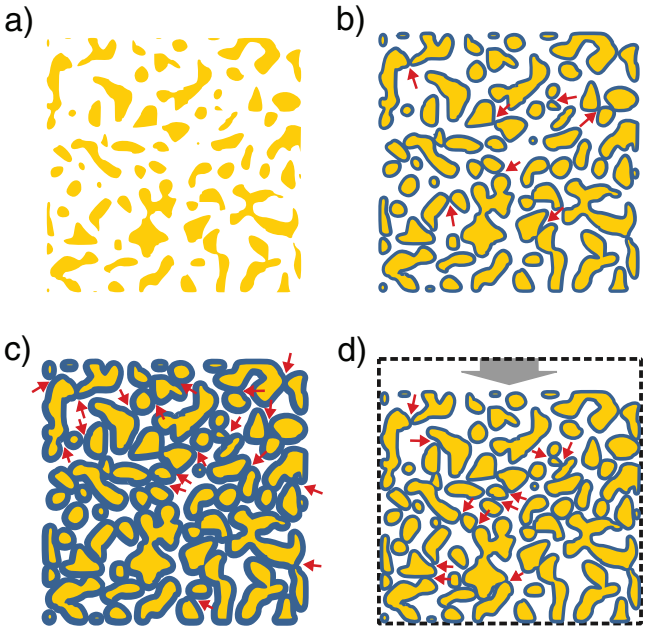

Figure 12. Different possibilities to create new connections between adjacent ligaments. a) Cross-sectional overview of bare nanoporous gold (NPG). b) Cross-section with intermediate amount of polypyrrole (PPy) on the NPG substrate. Several ligaments have been linked by new PPy connections. c) Cross-section with high amount of PPy. Additional new connections have been formed. d) Deformed cross-section with intermediate amount of PPy. Connections are formed as consequence of the loss in volume. Arrows: examples for new connections.

Au phase fraction below $\varphi_{Au} = 0.3$ is coarsened.[65] The dome-shaped features in Figure 11 can be identified as remnants of such reconnections. Obviously, these connections ruptured when the specimen was cleaved.

Because PPy bridges between neighboring ligaments appear to be abundant, we are led to inspect their contribution to the overall actuation. As illustrated in **Figure 12**a–c, more and more connections can be expected as the PPy phase fraction increases. The network of NPG contains disconnections[44,55,66] and has a significant tortuosity.[67,68] This leads to long and flexible load-bearing paths in-between the network's connecting nodes.[56,69] The resulting compliance implies that the dilation within the PPy bridges may quite efficiently deform the network. These considerations support the notion that the deformation normal to the ligament surface is transferred in the PPy bridges and plays a major role in macroscopic strain. This normal deformation acts in addition to the tangential deformation. Along with the number of bridges, its amount must increase with the PPy phase fraction. Thereby, the contribution of the PPy bridges explains qualitatively the unexpected increase of A^* with φ_{PPy}.

A consequence of the above suggestion is that the actuation coefficient should increase when the sample is plastically compressed. This expectation is based on the notion that additional bridges are formed when the densification moves neighboring ligaments toward each other. Figure 12d illustrates this process.

We tested the notion of contact formation by densification by exploring the variation of A^* while the hybrid material was plastically compressed. Figure 9d shows the results. The increase of A^* upon plastic deformation is striking. The confirmation of our prediction supports the notion that the newly formed connections contribute strongly to the actuation. As verification, we inspect the data for the NPG reference sample in the same figure. Even though the densification must result in new contacts between neighboring ligaments, A^* does not increase. This observation conforms with our scenario, because the actuation of NPG originates exclusively from the surface stress, thus from the tangential stresses in the outermost atomic layer of the metal. The significant expansion of the PPy coating along the surface normal has no equivalent in bare NPG. This is consistently confirmed by our experimental data.

5.3. Response Time

A central finding in this work is that mm-sized monolithic bodies of our gold–PPy–electrolyte hybrid material have response times for actuation around 2 s. We now compare this observation to the kinetics of bare PPy.

As mentioned in Section 1, the charging kinetics of oxidized PPy follows the classical $t = x^2 D^{-1}$ diffusion law, where x is the diffusion path length and D is the ion diffusion coefficient. For aqueous ClO_4^- in PPy, D is in the order of 2×10^{-9} cm^2 s^{-1}.[25,70] This is consistent with fast actuation by thin PPy films; for 100 nm and 1 µm thickness, the estimated equilibration times are in the order of several 10 ms and seconds, respectively. Yet, for a dense PPy body with a diffusion path length of 0.5 mm—comparable to the dimensions of our samples—the above diffusion law suggests a response time in the order of 10^6 s or about 300 h, too slow for practical applications. However, with $D = 1.5 \times 10^{-5}$ cm^2 s^{-1},[71] the diffusion of ClO_4^- is four orders of magnitude faster in water than in PPy. For a process mediated by ion diffusion in water with a diffusion path length of 0.5 mm, the estimate for the equilibration time would decrease to 10^2s. This illustrates the potential to accelerate the actuation of PPy by incorporating it into the design scheme of a hybrid material with a stiff metal skeleton for the electrical conductivity and load transfer, the PPy for the chemo-electro-mechanical coupling, and electrolyte-filled pore channels for the fast long-range ion transport.

The switching time of our material supports the above-mentioned scheme. In fact, we find response times even shorter than estimated. As a conceivable and speculative explanation, the fast reaction might reflect the combination of a short-range and fast local ion exchange between the PPy and the aqueous electrolyte in the pore space, while the long-range charge transport—which is required for charge neutrality—is carried by the Grotthuss mechanism.[72] By virtue of its accelerated actuation, our material enables monolithic macroscopic actuators using PPy as the active component. The advantage of this actuator geometry is that it can work against compressive loads in a freestanding geometry.

A consequence of our materials design scheme is that, as long as the interconnected pore space is available for ion transport in the electrolyte, the characteristic values A^*, Y, and σ_Y are enhanced with increasing φ_{PPy}. Yet, the extreme case of a complete filling of the pores with PPy would result in the loss of the liquid phase ion transport and yield slow reaction times similar to that of bulk PPy. This emphasizes that a minimum of porosity is required.

© 2020 The Authors. Advanced Materials Interfaces published by Wiley-VCH GmbH

5.4. Mechanical Work Density

An important figure of merit of actuators is the mechanical work which can be performed against an external load. For linear elastic actuators, the work density (per volume of the actuator), w_V, depends on Young's modulus and on the maximum actuation strain, $w_V = 1/4\, Y\varepsilon_{max}^2$.[73] Because w_V scales quadratically with ε_{max}, the up to 100-fold increase in strain amplitude of the PPy coated specimens implies an up to 10^4-fold increase of w_V.

After 13.6% plastic deformation, the specimen with $\varphi_{PPy} = 0.30$ exhibits a peak-to-peak strain amplitude of $\varepsilon_{max} = 0.51\%$ and a stiffness of 1030 MPa. The estimated work density is $w_V = 6.7\,\mathrm{kJ\,m^{-3}}$. Considering the work done by the volume change, the work density triples to $w_V^{3D} = 20.1\,\mathrm{kJ\,m^{-3}}$, because the dilatation of the nanoporous specimens is isotropic. Lead zirconium titanate (PZT) actuators have a typical stiffness $Y < 70$ GPa[74,75] and a typical strain amplitude <0.1%.[76–78] Using these values, the work density is estimated as $w_V < 17.5\,\mathrm{kJ\,m^{-3}}$. The PPy system used in this work has been thoroughly studied and its stiffness was determined to be $Y = 500$ MPa.[12] With a typical strain amplitude of 1–2%,[3,5,21,79] the work density of freestanding PPy emerges to $w_V = 12.5$ to $50\,\mathrm{kJ\,m^{-3}}$ or $w_V^{3D} = 37.5$ to $150\,\mathrm{kJ\,m^{-3}}$.

Young's modulus of our hybrid material is less than that of piezoceramics and similar to that of PPy. The work densities are comparable and the NPG-PPy hybrids exhibit larger strain amplitudes than piezoceramics, whereas they are generally less than for PPy. Even though the work density is highest for PPy, using bare PPy as a massive, free-standing actuator would require thick cross-sections in order to bear significant loads. The slow reaction times of such actuators limit possible fields of application considerably.

6. Conclusion

This work presents a deposition protocol that enables a conformal polypyrrole (PPy) coating within the inner pore space of mm-sized monolithic bodies of nanoporous gold (NPG) made by dealloying. The characteristic microstructural length scale of the metal skeleton can be as small as 120 nm, providing for enhanced strength. With the remaining pore space filled with aqueous electrolyte, the material forms a metal–PPy–electrolyte hybrid material in which the metal skeleton provides the strength and the electrical conductivity, the PPy the chemo-electro-mechanical coupling for actuation, and the aqueous electrolyte the fast ion transport. Our material reaches peak-to-peak strain amplitudes in the order of 0.5%. This is less than with bare PPy, but more than with commercial piezoceramics.

The central findings are as follows: Our experiments show that the hybrid material of this study offers a) an enhanced strength compared to earlier NPG-based hybrids, owing to its fine microstructural length scale and to the conditioning by plastic deformation, b) fast actuation of 3D, mm-sized geometries due to the fast transport in the electrolyte channels, and c) actuation of freestanding bodies of the actuator material under compressive loads owing to the strength of the metal skeleton. Furthermore, d) a comparison of the mechanical properties and the actuation of the hybrid material to the bare metal skeleton enables a detailed discussion of the micromechanics which governs the transfer of the stress and the strain from the PPy into the skeleton. This mechanical interaction defines the macroscopic actuation of the material.

The metal skeleton in our material consists of nanoporous gold. NPG is a suitable model material, because its mechanical and actuation properties have been extensively studied. Obviously, the high cost of gold makes the material poorly suitable for applications. Yet, our functionalization strategy may readily be transferred to technologically more relevant materials. Nanoporous copper,[80,81] nanoporous copper-nickel alloys,[82] or microporous titanium[83–85] have been demonstrated and may form alternatives for the skeleton structure. Thus, our study may be a first step toward the application of PPy in mm-sized actuators.

Supporting Information

Supporting Information is available from the Wiley Online Library or from the author.

Acknowledgements

This work was funded by the Deutsche Forschungsgemeinschaft (DFG, German Research Foundation)—project number 192346071—SFB 986.
Open access funding enabled and organized by Projekt DEAL.

Conflict of Interest

The authors declare no conflict of interest.

Keywords

actuation, nanoporous gold, polypyrrole, strain-charge coupling

Received: August 12, 2020
Revised: September 29, 2020
Published online: November 4, 2020

[1] Q. Pei, O. Inganäs, *J. Phys. Chem.* **1992**, *96*, 10507.
[2] Q. Pei, O. Inganäs, *Solid State Ionics* **1993**, *60*, 161.
[3] A. Mazzoldi, A. Della Santa, D. De Rossi, *Polymer Sensors and Actuators*, Springer, Cham, Switzerland **2000**, pp. 207–244.
[4] L. Bay, T. Jacobsen, S. Skaarup, K. West, *J. Phys. Chem. B* **2001**, *105*, 8492.
[5] J. D. Madden, P. G. Madden, I. W. Hunter, *Proc. SPIE* **2002**, *4695*, 176.
[6] T. F. Otero, J. Martínez, B. Zaifoglu, *Smart Mater. Struct.* **2013**, *22*, 104019.
[7] E. D. Daneshvar, E. Smela, *Adv. Healthcare Mater.* **2014**, *3*, 1026.
[8] L. Valero, T. F. Otero, J. G. Martínez, *ChemPhysChem* **2014**, *15*, 293.
[9] M. Kaneko, M. Fukui, W. Takashima, K. Kaneto, *Synth. Met.* **1997**, *84*, 795.
[10] A. Hutchison, T. Lewis, S. Moulton, G. Spinks, G. Wallace, *Synth. Met.* **2000**, *113*, 121.
[11] J. D. Madden, P. G. Madden, I. W. Hunter, *Proc. SPIE* **2001**, *4329*, 72.

© 2020 The Authors. Advanced Materials Interfaces published by Wiley-VCH GmbH

[12] T. F. Otero, J. L. Cascales, G. V. Arenas, *Mater. Sci. Eng. C* **2007**, *27*, 18.
[13] T. A. Skotheim, J. Reynolds, *Handbook of Conducting Polymers*, CRC Press, CRC Press **2007**.
[14] T. Shoa, J. D. Madden, T. Mirfakhrai, G. Alici, G. M. Spinks, G. G. Wallace, *Sens. Actuators, A* **2010**, *161*, 127.
[15] J. D. Madden, R. A. Cush, T. S. Kanigan, I. W. Hunter, *Synth. Met.* **2000**, *113*, 185.
[16] E. Smela, N. Gadegaard, *J. Phys. Chem. B* **2001**, *105*, 9395.
[17] S. Hara, T. Zama, W. Takashima, K. Kaneto, *Synth. Met.* **2005**, *149*, 199.
[18] S. Hara, T. Zama, W. Takashima, K. Kaneto, *Synth. Met.* **2006**, *156*, 351.
[19] R. Baughman, *Synth. Met.* **1996**, *78*, 339.
[20] T. F. Otero, M. Cortes, *Chem. Commun.* **2004**, 284.
[21] P. Chiarelli, A. D. Santa, D. De Rossi, A. Mazzoldi, *J. Intell. Mater. Syst. Struct.* **1995**, *6*, 32.
[22] P. A. Anquetil, D. Rinderknecht, N. A. Vandesteeg, J. D. Madden, I. W. Hunter, *Smart Structures and Materials: Electroactive Polymer Actuators and Devices (EAPAD)*, Vol. *5385*, SPIE, Washington DC **2004**, p. 380–388.
[23] B. Roschning, J. Weissmüller, *Electrochim. Acta* **2019**, *318*, 504.
[24] T. F. Otero, H.-J. Grande, J. Rodríguez, *J. Phys. Chemi. B* **1997**, *101*, 3688.
[25] I. J. Suarez, T. F. Otero, M. Marquez, *J. Phys. Chem. B* **2005**, *109*, 1723.
[26] R. Khadka, Z. Zondaka, A. Kesküla, M. S. Khorram, T. T. Khanh, T. Tamm, J. Travas-Sejdic, R. Kiefer, *J. Appl. Polym. Sci.* **2018**, *135*, 46831.
[27] E. Smela, O. Inganäs, I. Lundström, *Science* **1995**, *268*, 1735.
[28] E. Smela, *Adv. Mater.* **2003**, *15*, 481.
[29] S. Assavapanumat, B. Gupta, G. Salinas, B. Goudeau, C. Wattanakit, A. Kuhn, *Chem. Commun.* **2019**, *55*, 10956.
[30] M. Pyo, C. C. Bohn, E. Smela, J. R. Reynolds, A. B. Brennan, *Chem. Mater.* **2003**, *15*, 916.
[31] T. F. Otero, J. Martinez, J. Arias-Pardilla, *Electrochim. Acta* **2012**, *84*, 112.
[32] K. K. Lee, Y. Dobashi, P. R. Herman, J. D. Madden, V. X. Yang, *Smart Mater. Struct.* **2018**, *28*, 015028.
[33] R. Kiefer, P. A. Kilmartin, G. A. Bowmaker, R. P. Cooney, J. Travas-Sejdic, *Sens. Actuators, B* **2007**, *125*, 628.
[34] D. Melling, S. Wilson, E. W. Jager, *Smart Mater. Struct.* **2013**, *22*, 104021.
[35] B. Gupta, B. Goudeau, A. Kuhn, *Angew. Chem., Int. Ed.* **2017**, *56*, 14183.
[36] B. Gupta, B. Goudeau, P. Garrigue, A. Kuhn, *Adv. Funct. Mater.* **2018**, *28*, 1705825.
[37] T. I. Schnoor, U. Vainio, L.-H. Shao, E. T. Lilleodden, M. Müller, A. Schreyer, K. Schulte, B. Fiedler, *Adv. Eng. Mater.* **2016**, *18*, 597.
[38] M. Beregoi, A. Evanghelidis, V. C. Diculescu, H. Iovu, I. Enculescu, *ACS Appl. Mater. Interfaces* **2017**, *9*, 38068.
[39] K. Wang, C. Stenner, J. Weissmüller, *Sens. Actuators, B* **2017**, *248*, 622.
[40] J. Biener, A. M. Hodge, J. R. Hayes, C. A. Volkert, L. A. Zepeda-Ruiz, A. V. Hamza, F. F. Abraham, *Nano Lett.* **2006**, *6*, 2379.
[41] A. Mathur, J. Erlebacher, *Appl. Phys. Lett.* **2007**, *90*, 061910.
[42] A. Hodge, J. Biener, J. Hayes, P. Bythrow, C. Volkert, A. Hamza, *Acta Mater.* **2007**, *55*, 1343.
[43] M. Hakamada, M. Mabuchi, *Scr. Mater.* **2007**, *56*, 1003.
[44] N. Mameka, K. Wang, J. Markmann, E. T. Lilleodden, J. Weissmüller, *Mater. Res. Lett.* **2016**, *4*, 27.
[45] H.-J. Jin, J. Weissmüller, D. Farkas, *MRS Bull.* **2018**, *43*, 35.
[46] H.-J. Jin, S. Parida, D. Kramer, J. Weissmüller, *Surf. Sci.* **2008**, *602*, 3588.
[47] L. Lührs, C. Soyarslan, J. Markmann, S. Bargmann, J. Weissmüller, *Scr. Mater.* **2016**, *110*, 65.
[48] A. J. Bard, L. R. Faulkner, *Electrochemical Methods: Fundamentals and Applications*, 2nd ed., John Wiley and Sons, Inc., New York **2001**.
[49] T. F. Otero, J. G. Martinez, *J. Solid State Electrochem.* **2011**, *15*, 1169.
[50] T. Lewis, G. Wallace, C. Kim, D. Kim, *Synth. Met.* **1997**, *84*, 403.
[51] B. Conway, W. Pell, *J. Solid State Electrochem.* **2003**, *7*, 637.
[52] J. Tanguy, N. Mermilliod, M. Hoclet, *J. Electrochem. Soc.* **1987**, *134*, 795.
[53] N. Fekri, J. D. Madden, N. Y.-J. Lee, F. Ko, C. A. Michal, *Synth. Met.* **2014**, *187*, 145.
[54] S. Trasatti, O. Petrii, *J. Electroanal. Chem.* **1992**, *327*, 353.
[55] L.-Z. Liu, X.-L. Ye, H.-J. Jin, *Acta Mater.* **2016**, *118*, 77.
[56] M. Ziehmer, K. Hu, K. Wang, E. T. Lilleodden, *Acta Mater.* **2016**, *120*, 24.
[57] Y.-c. K. Chen-Wiegart, S. Wang, Y. S. Chu, W. Liu, I. McNulty, P. W. Voorhees, D. C. Dunand, *Acta Mater.* **2012**, *60*, 4972.
[58] D. Kramer, R. N. Viswanath, J. Weissmüller, *Nano Lett.* **2004**, *4*, 793.
[59] N. Vasiljevic, T. Trimble, N. Dimitrov, K. Sieradzki, *Langmuir* **2004**, *20*, 6639.
[60] M. Smetanin, R. Viswanath, D. Kramer, D. Beckmann, T. Koch, L. Kibler, D. Kolb, J. Weissmüller, *Langmuir* **2008**, *24*, 8561.
[61] M. Lafouresse, U. Bertocci, C. Beauchamp, G. Stafford, *J. Electrochem. Soc.* **2012**, *159*, H816.
[62] J. Weissmüller, H.-L. Duan, D. Farkas, *Acta Mater.* **2010**, *58*, 1.
[63] W. Martienssen, H. Warlimont, *Springer Handbook of Condensed Matter and Materials Data*, Springer Science & Business Media, Berlin, Heidelberg **2006**.
[64] E. Smela, M. Kallenbach, J. Holdenried, *J. Microelectromech. Syst.* **1999**, *8*, 373.
[65] Y. Li, B.-N. Dinh Ngô, J. Markmann, J. Weissmüller, *Phys. Rev. Mater.* **2019**, *3*, 076001.
[66] L.-Z. Liu, H.-J. Jin, *Appl. Phys. Lett.* **2017**, *110*, 211902.
[67] Y. Xue, J. Markmann, H. Duan, J. Weissmüller, P. Huber, *Nat. Commun.* **2014**, *5*, 4237.
[68] J. Jiao, N. Huber, *Comput. Mater. Sci.* **2017**, *127*, 194.
[69] K. Hu, M. Ziehmer, K. Wang, E. T. Lilleodden, *Philos. Mag.* **2016**, *96*, 3322.
[70] X. Ren, P. G. Pickup, *J. Phys. Chem.* **1993**, *97*, 5356.
[71] S. R. Heil, M. Holz, T. M. Kastner, H. Weingärtner, *J. Chem. Soc., Faraday Trans.* **1995**, *91*, 1877.
[72] N. Agmon, *Chem. Phys. Lett.* **1995**, *244*, 456.
[73] H.-J. Jin, X.-L. Wang, S. Parida, K. Wang, M. Seo, J. Weissmüller, *Nano Lett.* **2010**, *10*, 187.
[74] A. J. Moulson, J. M. Herbert, *Electroceramics: Materials, Properties, Applications*, John Wiley & Sons, New York **2003**.
[75] S. J. Rupitsch, *Piezoelectric Sensors and Actuators*, Springer, Berlin, Germany **2019**.
[76] I. W. Hunter, S. Lafontaine, *Technical Digest IEEE Solid-State Sensor and Actuator Workshop*, IEEE, Piscataway, NJ **1992**, pp. 178–185.
[77] Q. Zhang, V. Bharti, X. Zhao, *Science* **1998**, *280*, 2101.
[78] J. Rödel, W. Jo, K. T. Seifert, E.-M. Anton, T. Granzow, D. Damjanovic, *J. Am. Ceram. Soc.* **2009**, *92*, 1153.
[79] A. Della Santa, D. De Rossi, A. Mazzoldi, *Synth. Met.* **1997**, *90*, 93.
[80] Z. Qi, C. Zhao, X. Wang, J. Lin, W. Shao, Z. Zhang, X. Bian, *J. Phys. Chem. C* **2009**, *113*, 6694.
[81] X. Li, B. Huang, C. Qiu, Z. Li, L.-H. Shao, H. Liu, *J. Alloys Compd.* **2016**, *681*, 109.
[82] L. Lührs, J. Weissmüller, *Scr. Mater.* **2018**, *155*, 119.
[83] T. Wada, K. Yubuta, A. Inoue, H. Kato, *Mater. Lett.* **2011**, *65*, 1076.
[84] M. Tsuda, T. Wada, H. Kato, *J. Appl. Phys.* **2013**, *114*, 113503.
[85] I. Okulov, J. Weissmüller, J. Markmann, *Sci. Rep.* **2017**, *7*, 20.

© 2020 The Authors. Advanced Materials Interfaces published by Wiley-VCH GmbH